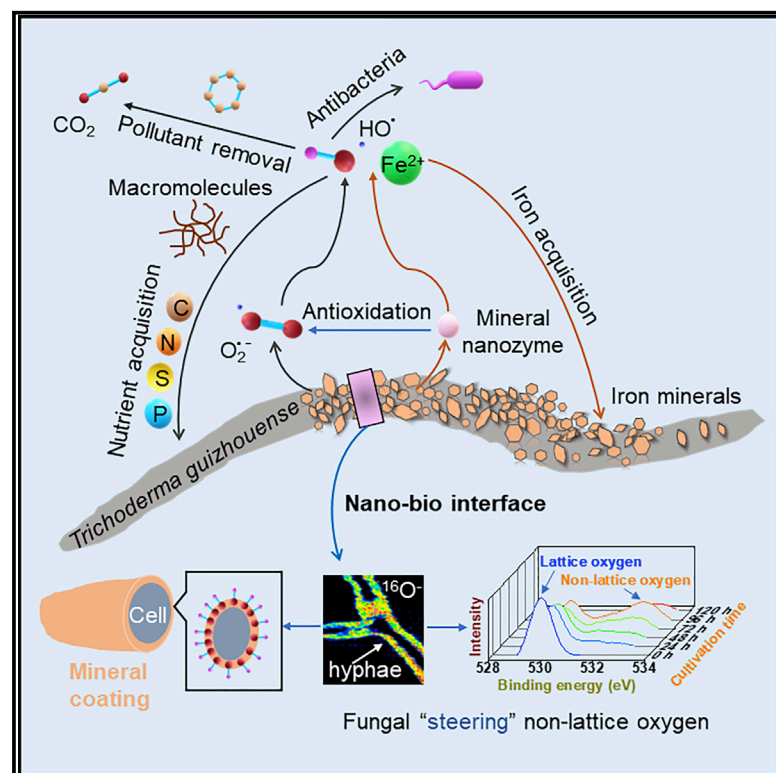


# Fungal Nanophase Particles Catalyze Iron Transformation for Oxidative Stress Removal and Iron Acquisition

## Graphical Abstract



## Authors

Guang-Hui Yu, Zhi-Lai Chi, Andreas Kappler, Fu-Sheng Sun, Cong-Qiang Liu, Hui Henry Teng, Geoffrey Michael Gadd

## Correspondence

yuguanghui@tju.edu.cn (G.-H.Y.),  
huihenry.teng@tju.edu.cn (H.H.T.),  
g.m.gadd@dundee.ac.uk (G.M.G.)

## In Brief

Yu et al. show that biogenic ferrihydrite nanoparticles, formed by fungal interaction with hematite, performed as mimetic catalysts, similar to nanozymes that imitate peroxidase. Non-lattice oxygen was mainly responsible for this catalytic activity. This work provides insights into pathways controlling the evolution of biogenic mineral formation.

## Highlights

- Biogenic ferrihydrite nanoparticles were formed during fungus-hematite interactions
- Biogenic ferrihydrite nanoparticles can perform as catalysts that imitate peroxidase
- Non-lattice oxygen in the nanomaterials was responsible for the catalytic activity



## Article

# Fungal Nanophase Particles Catalyze Iron Transformation for Oxidative Stress Removal and Iron Acquisition

Guang-Hui Yu,<sup>1,7,\*</sup> Zhi-Lai Chi,<sup>2,7</sup> Andreas Kappler,<sup>3</sup> Fu-Sheng Sun,<sup>1</sup> Cong-Qiang Liu,<sup>1</sup> Hui Henry Teng,<sup>1,4,\*</sup> and Geoffrey Michael Gadd<sup>5,6,8,\*</sup>

<sup>1</sup>Institute of Surface-Earth System Science, School of Earth System Science, Tianjin University, Tianjin 300072, China

<sup>2</sup>College of Resources & Environmental Sciences, Nanjing Agricultural University, Nanjing 210095, China

<sup>3</sup>Geomicrobiology, Center for Applied Geosciences, University of Tübingen, Tübingen 72076, Germany

<sup>4</sup>Department of Chemistry, George Washington University, Washington, DC 20006, USA

<sup>5</sup>Geomicrobiology Group, School of Life Sciences, University of Dundee, Dundee DD1 5EH, Scotland, UK

<sup>6</sup>State Key Laboratory of Heavy Oil Processing, Beijing Key Laboratory of Oil and Gas Pollution Control, College of Chemical Engineering and Environment, China University of Petroleum, Beijing 102249, China

<sup>7</sup>These authors contributed equally

<sup>8</sup>Lead Contact

\*Correspondence: [yuguanghui@tju.edu.cn](mailto:yuguanghui@tju.edu.cn) (G.-H.Y.), [huihenry.teng@tju.edu.cn](mailto:huihenry.teng@tju.edu.cn) (H.H.T.), [g.m.gadd@dundee.ac.uk](mailto:g.m.gadd@dundee.ac.uk) (G.M.G.)

<https://doi.org/10.1016/j.cub.2020.05.058>

## SUMMARY

Microbe-mineral interactions have shaped the surface of the Earth and impacted the evolution of plants and animals. Although more than two-thirds of known mineral species have biological imprints, how the biotransformation of minerals may have benefited microbial development, beyond nutritional and energetic use, remains enigmatic. In this research, we have shown that biogenic ferrihydrite nanoparticles are extensively formed at the interface between an actively growing fungus and an iron-containing mineral, hematite. These biogenic nanoparticles formed through the fungus-hematite interactions can behave as mimetic catalysts, similar to nanozymes that imitate peroxidase, which scavenges hydrogen peroxide for the mitigation of potential cytotoxicity. Evidence from various X-ray spectroscopic analyses indicated that non-lattice oxygen in the nanomaterials was chiefly responsible for this catalytic activity, rather than through the conventional mechanisms of iron redox chemistry. Cryo-scanning electron microscopy, high-resolution (~30 nm) 3D volume rendering, and biomass analyses further confirmed that the organism was active and capable of mediating the catalytic reactions. We therefore hypothesize that this confers an advantage to the organism in terms of protection from oxidative stress and ensuring the acquisition of essential iron. This work raises new questions about the roles of biogenic nanomaterials in the coevolution of the lithosphere and biosphere and provides a step toward understanding the feedback pathways controlling the evolution of biogenic mineral formation.

## INTRODUCTION

Synthetic nanomaterials have recently been found to exhibit enzyme-like catalytic activities (hence the term nanozymes) that can facilitate various biochemical reactions that have been utilized for immunoassays, biosensing, and medical diagnoses [1–3]. This unique reactivity, if occurring in naturally occurring minerals, may mean that inorganic geomaterials are an unnoticed contributor to the evolution of the biosphere [3]. Among the minerals that can potentially act as nanozymes, ferrihydrite (ideal formula  $\text{Fe}_{10}\text{O}_{14}(\text{OH})_2$ ) is of particular interest because of the mineral's ubiquitous presence in the Earth's surface [4, 5] and the known catalytic properties of iron (oxyhydr)oxide nanoparticles that imitate natural peroxidase, an antioxidant enzyme pivotal for the removal of excess reactive oxygen species (ROS), such as superoxide ( $\text{O}_2^{\cdot-}$ ) and hydrogen peroxide ( $\text{H}_2\text{O}_2$ ), in biological systems to ameliorate oxidative stress and maintain cellular redox balance [1–3].

In this work, we have investigated the fungal formation of ferrihydrite (iron(III) oxyhydroxide) and this biogenic mineral's nanozyme-like activity, using *Trichoderma guizhouense* NJAU4742 and hematite ( $\alpha\text{-Fe}_2\text{O}_3$ ) as the model system [6, 7]. The Fungi joined microbe-Earth coevolution nearly 2 Ga later relative to the earliest life forms [8, 9] but were instrumental in the onset of land colonization by photosynthetic eukaryotes, such as plants [10]. Fungus-mineral interactions play key roles in rock, mineral, and metal transformations; rhizospheric organic matter degradation; and phosphate fixation [9], but resultant secondary mineral phases, particularly biogenic nanoparticles [11, 12], have not been linked to any obvious biological functions. Furthermore, fungal production of extracellular  $\text{O}_2^{\cdot-}$  and  $\text{H}_2\text{O}_2$  during growth has been extensively reported [6, 12, 13], yet the processes required to combat the ensuing potential oxidative stress remain to be fully elucidated [14]. The objectives of this work were therefore to (1) examine the biogenic formation of ferrihydrite nanoparticles during fungus-hematite interactions and (2) test



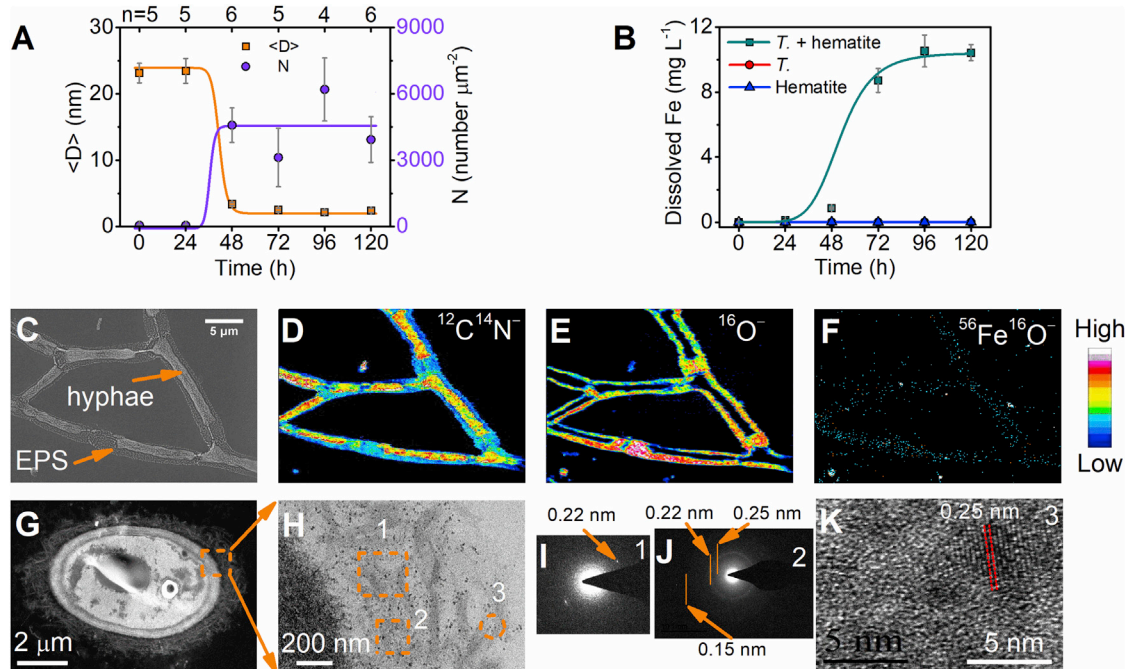


**Figure 1. Fungal Biotransformation of Hematite to Ferrihydrate Nanoparticles**

(A) Changes of mean particle size ( $\langle D \rangle$ ) and number (N) of ferrihydrate nanoparticles in media derived from transmission electron microscopy (TEM). See also Data S1.

(B) Changes in dissolved Fe during the fungal-mineral cultivation. Detailed descriptions of total and structural  $\text{Fe}^{2+}$  are summarized in Table S1 and Data S5.

(C) Extracellular polymeric substances (EPS) revealed by scanning electron microscopy (SEM).

(D)  $^{12}\text{C}^{14}\text{N}^-$  secondary ion image as analyzed via NanoSIMS. See also Figure S1.

(E)  $^{16}\text{O}^-$  secondary ion image as analyzed via NanoSIMS. See also Figure S1.

(F)  $^{56}\text{Fe}^{16}\text{O}^-$  secondary ion image as analyzed via NanoSIMS. See also Figure S1.

(G) Cross-sectional view of a hypha obtained using HAADF-STEM. See also Figure S2.

(H) TEM image. See also Figure S2.

(I and J) Fast Fourier transform (FFT) of ferrihydrate nanoparticles. See also Figure S2.

(K) High-resolution TEM (HRTEM) image of ferrihydrate nanoparticles. See also Figure S2.

whether the biogenic ferrihydrate nanoparticles can imitate peroxidase to scavenge hydrogen peroxide for the potential mitigation of cytotoxicity. Through systematically scrutinizing the model fungal-mineral interactions, our results have provided crucial insights into the possible mechanisms underlying coevolution of the lithosphere and biosphere and provide a foundation for fundamental research on the potential importance of mineral nanozymes to microbial evolution.

## RESULTS

### Iron (Oxyhydr)oxide Nanoparticle Formation during Fungus-Mineral Cultivation

During fungus-mineral cultivation, transmission electron microscopy (TEM) revealed that the mineral grains (from the initial hematite particles) experienced an 8-fold size reduction, giving rise to a high-density distribution (3,000–6,000 per  $\mu\text{m}^{-2}$ ; Figure 1A) of  $\sim 3$ -nm-sized nanoparticles in the aggregates within 48 h. Analysis of the solution chemistry of the media showed a monotonic increase of dissolved Fe, dominated by  $\text{Fe}^{2+}$  (Table S1), over the first 96 h before reaching a plateau near the end of the 120-h incubation period (Figure 1B). This increase was particularly pronounced after 48 h, probably due to the  $<20$ -nm particles

being interpreted as “dissolved” Fe by the analytical technique used [8]. By comparison, such trends were not found in control experiments (medium with only fungus or hematite; Figure 1B), confirming that the fungal-mineral interaction was necessary for nanoparticle formation.

Detailed examination of the mycelium-mineral aggregates by correlative scanning electron microscopy (SEM) (Figure 1C) and nanoscale secondary ion mass spectrometry (NanoSIMS) (Figures 1C–1E and S1) revealed the existence of a matrix of extracellular polymeric substances (EPSs) (Figures 1C and 1D) enveloping the hyphae at the end of the cultivation period. Previous work has shown that  $^{56}\text{Fe}^{16}\text{O}^-$  is indicative of Fe-enriched phases and  $^{16}\text{O}^-$  represents mineral phases [15]. The profound intensity of  $^{16}\text{O}^-$  in the EPS matrix was interpreted to be a strong signal of mineral phases (Figure 1E), whereas the unmistakable  $^{56}\text{Fe}^{16}\text{O}^-$  signal (Figure 1F), together with high-angle annular dark-field scanning TEM (HAADF-STEM) imaging of 70-nm- and 30-nm-thick hyphal sections and culture solution (Figures 1G and S2), indicated the presence of intracellular Fe (blue dots in Figure 1F and white regions in Figures 1G and S2) and therefore the acquisition of essential iron by the fungus. Selected area electron diffraction (SAED) (Figures 1I, 1J, and S2), high-resolution TEM (HRTEM) (Figure 1K), and energy-dispersive

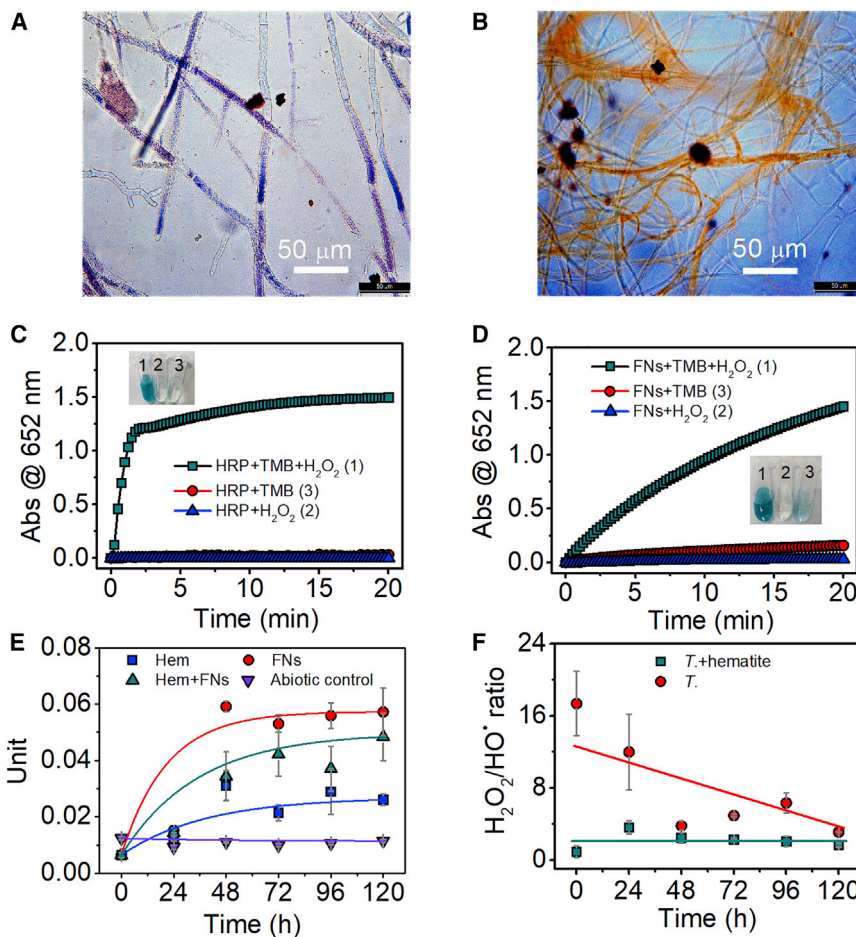


**Figure 2. Enzyme-like Activities of Biogenic Ferrihydrite Nanoparticles**

(A and B) Location of  $\text{H}_2\text{O}_2$  (blue in A) and  $\text{O}_2^{\cdot-}$  (brown in B) in hyphae shown by staining. (C and D) Progress and yield of the TMB colorimetric reaction catalyzed by 50 ng/mL horseradish peroxidase (HRP) (C) in comparison to that catalyzed by FNs (D). See also Figure S3 and Data S2. (E) Variation of peroxidase-like activity in culture with hematite, hematite + EPS, FNs, and the abiotic control (i.e., hematite exposed to a pH of 3.6;  $n = 3$ ). See also Figure S3 and Data S2. (F) Relative abundance of  $\text{H}_2\text{O}_2$  versus  $\text{HO}^{\cdot}$  in culture with and without FNs ( $n = 2$  or 3). See also Figures S3 and S4 and Data S4.

as catalytically active as the synthetic ferrihydrite nanozyme (0.06 versus 0.12 units) but were an order of magnitude more efficient than both the synthetic hematite (0.006 units) and the hematite in the abiotic control (i.e., the hematite exposed to a similar pH as the FNs; 0.003) used as the parental mineral (Figures 2E and S3). Consistent with the onset of nanoparticle production (Figure 1A), the peroxidase-like activity in the culture exhibited the strongest increase from 24 to 48 h (Figure 2E).

Direct measurements of  $\text{H}_2\text{O}_2$  and hydroxyl radical ( $\text{HO}^{\cdot}$ ) content further validated the FNs' peroxidase-like activity (Figure S3). First,  $\text{H}_2\text{O}_2$  and  $\text{HO}^{\cdot}$  were

X-ray spectroscopy (EDS) analyses (Figure S2) all indicated that the EPS-bound mineral phase comprised poorly crystalline nanoparticles with an interplanar distance of 0.22 nm, two broad rings at 0.15 and 0.25 nm, and a lattice spacing of 0.25 nm, which was consistent with 2-line ferrihydrite [12, 16]. Collectively, these multiple lines of evidence signified strong fungal production of extracellular ferrihydrite nanoparticles (FNs) that were closely associated with the mycelium through the EPS matrix.

### Iron (Oxyhydr)oxide Nanoparticles Acting as a Mimetic Peroxidase Catalyzing ROS Reactions

The production of ROS during fungal growth was confirmed by nitroblue tetrazolium (NBT) and 3,3'-diaminobenzidine (DAB) staining [13], which showed concentrated  $\text{O}_2^{\cdot-}$  at the hyphal tips and a diffuse  $\text{H}_2\text{O}_2$  distribution along the hyphae (Figures 2A and 2B). Because  $\text{O}_2^{\cdot-}$  is usually static, whereas  $\text{H}_2\text{O}_2$  is mobile upon formation (up to 1 mm migration) [17], we postulate that  $\text{H}_2\text{O}_2$  was first formed at the hyphal tips by dismutation of  $\text{O}_2^{\cdot-}$ , which subsequently diffused along the hyphae (Figure 2B) and also into the media (Figure S3).

Tests using the classic 3,3',5,5'-tetramethylbenzidine (TMB) assay for peroxidase-catalyzed  $\text{H}_2\text{O}_2$  reduction [1, 2] showed that, at the end of the 120-h cultivation, the EPS-bound FNs exhibited a catalytic activity comparable to that of 50 ng/mL horseradish peroxidase (HRP) (Figures 2C and 2D). The FNs were not

maintained at near-zero levels throughout the abiotic control experiments, therefore dismissing the possibility of significant formation of  $\text{H}_2\text{O}_2$  and  $\text{HO}^{\cdot}$  by hematite-culture interactions (Figure S3). Second, in contrast to the early-stage predominance of  $\text{H}_2\text{O}_2$  over  $\text{HO}^{\cdot}$  during fungal growth in pure mineral-free media (Figure 2F), the presence of the mineral altered the solution chemistry so that the system maintained a  $\text{H}_2\text{O}_2$  to  $\text{HO}^{\cdot}$  ratio at a near-constant low level throughout the incubation period (Figure 2F). This finding directly attests to the occurrence of mimetic catalysis. Moreover, the effectiveness of such catalysis in the presence of increasing medium acidity (the pH decreased from  $\sim 5.4$  to  $\sim 2.0$  during cultivation, regardless of the presence of hematite; Figure S3) and micro-environmental acidity (the pH varying from  $\sim 6.5$  to  $< 4.5$ ; Figure S3) emphasized peroxidase- rather than catalase-mimicking (Figure 2F) reactions, as the latter only operates at pH-neutral conditions [2]. Together, these findings suggest that FNs plays a role in the regulation of oxidative stress in association with FN formation (Figure 2F).

### Catalytic Mechanism of the Biogenic Fe-Nanophases

Iron(II) is known to catalyze  $\text{H}_2\text{O}_2$  to  $\text{HO}^{\cdot}$  conversion through the Fenton reaction [12, 18]. Further, peroxidases often contain an iron-porphyrin derivative in their active sites. A natural extension from this knowledge is the assumption that the catalytic ability of the FNs was derived from Fe chemistry [19]. To test this

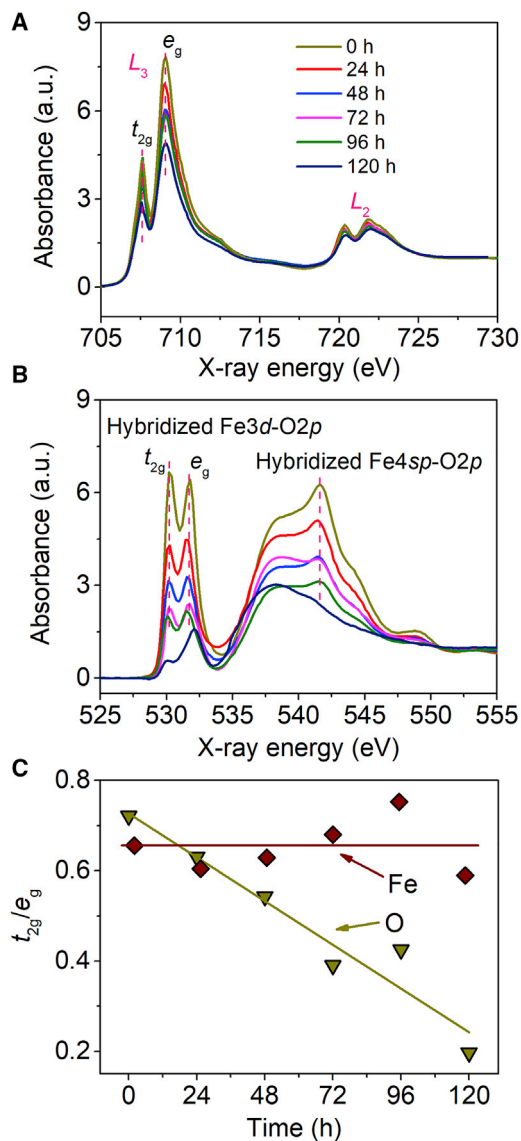


**Figure 3. Variation of Local Electronic Structures in Biogenic Ferrihydrite Nanoparticles**

(A and B) Time-dependent changes in Fe *L*-edge (A) and O *K*-edge (B) X-ray absorption spectroscopy (XAS) spectra. See also Figure S4 and Data S3.

(C) Time-dependent changes in the relative absorption intensity of the  $t_{2g}$  and  $e_g$  states for Fe and O. See also Figure S4 and Data S3.

hypothesis, we first examined time-dependent changes in Fe local electronic structures in the FNs using soft X-ray absorption spectroscopy (XAS) [20]. The Fe *L*-edge absorption (Figure 3A) corresponds to the excitation of Fe *2p* core electrons to unoccupied Fe *3d* states and is very sensitive to the oxidation state and the coordination environment of Fe [21]. The surface-sensitive total electron yield (TEY) spectra (Figure 3A) for Fe  $L_3$  absorption located at 707–710 eV exhibited a typical doublet structure, corresponding to  $t_{2g}$  and  $e_g$  states, respectively [20]. This forms  $e_g$  and  $t_{2g}$  molecular orbitals, which represent  $\sigma$  and  $\pi$  Fe–O bonds, respectively [20]. Although the absorption intensity of  $t_{2g}$  and  $e_g$  decreased over time, suggesting a decrease in Fe concentration

of the mineral, the ratio of the peak area ( $t_{2g}/e_g$ ) was maintained at a rather constant range of 0.60–0.75 throughout the experiments, signaling the absence of detectable changes in iron valency and coordination. However, the oxygen *K*-edge  $t_{2g}$  and  $e_g$  absorption weakened incongruently (Figure 3B), with  $t_{2g}/e_g$  declining by a factor of >3 over the 120-h cultivation (Figure 3C). This suggested a sizeable change in the oxygen-bonding environment over time [20]. By comparison,  $t_{2g}/e_g$  only changed by ~30% for hematite over the same time period (Figure S4).

The more pronounced changes in the O *K*-edge during iron oxide nanomaterial formation suggested that the chemistry of oxygen rather than iron controlled the peroxidase-mimicking activity of the FNs. The XAS signals of O *K*-edge  $t_{2g}$  and  $e_g$  in Fe-based perovskite were observed to show a dependence on the exerted overpotential, and this relationship was interpreted as the presence of electron holes that were charge balanced by the occurrence of oxygen vacancies  $O_V$  [20]. A recent study indeed found that engineered  $O_V$  in hematite can promote a surface electrocatalytic process through charge transfer enhancement [22]. Our X-ray photoelectron spectroscopy (XPS) measurements of oxygen-binding energy (Figures 4 and S4) in the FNs showed a 4-fold increase in intensity at ~532.2 eV and a concomitant decrease at ~530 eV associated with fungal cultivation, closely coupled with the pace of  $HO^\bullet$  increase in the system (Figure S3). Note that the peaks at 530 eV and 533.2 eV are assigned to lattice oxygen ( $O_L$ ) and non-lattice oxygen ( $O_{NL}$ ), respectively, with the latter being mainly derived from the contribution of hydroxyl (OH) at surface oxygen vacancy sites (hole [ $h^\bullet$ ]) [23]. Interestingly, the  $O_{NL}$  signal in FNs correlated with the  $HO^\bullet$  concentration in the media (Figures 4C and S4), suggesting a direct contribution of the surface OH of the mineral to the formation of hydroxyl radicals. Because of the increasing  $O_{NL}$  coinciding with the hematite to ferrihydrite phase transition during the experiments (Figures 1 and S4), we propose that the peroxidase-like activity of the FNs resides in the ability of  $O_V$  trapping and donating electrons [24] to facilitate charge transfer between the oxygens in  $H_2O_2$ .

### Hyphal Morphologies in the Absence or Presence of Iron Nanoparticles

To examine the effects of iron nanoparticles on fungal hyphae, cryo-SEM images of fungal biomass were conducted in the absence (Figures 5A and 5B) or in the presence (Figures 5C and 5D) of hematite. Our cryo-SEM images allow analysis of hydrated fungal-mineral samples (cultivated for 120 h), at temperatures down to  $-190^\circ C$ , and clearly showed that the fungal hyphae were intact after cultivation with hematite. Next, synchrotron radiation transmission X-ray microscopy (SR-TXM) imaging (Figure 5E; Video S1) showed the presence of iron minerals, pores, and fungal hyphae in fungal-mineral aggregates (120 h). To obtain further high-resolution images of fungal-mineral samples (120 h; Figure 5F), we performed a tilt series of 27 scanning transmission X-ray microscopy (STXM) images with soft X-ray energies at 706 eV and 710 eV, which are below and above the Fe  $L_3$  edge, respectively [25, 26]. These STXM images were rebuilt into 3D volume renderings using nanoscale computed microtomography (nano-CT) (Figures 5G and 5H). In high-resolution 3D volume renderings with a 30-nm-scale resolution (Figures 5G and 5H; Videos S2 and S3), Fe minerals with

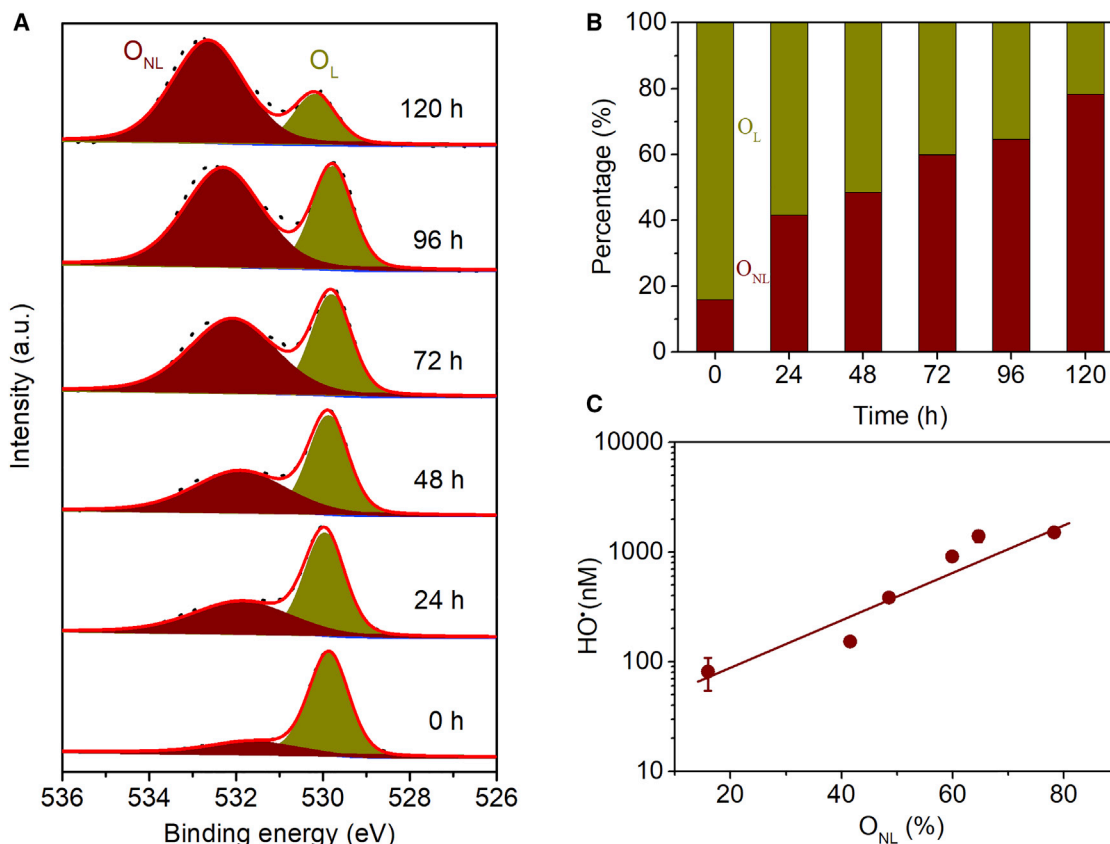


**Figure 4. Production of Non-lattice Oxygen in Ferrihydrite Nanoparticles Associated with Fungal-Mineral Cultivation**

(A) Rising O<sub>NL</sub> over time shown by the fine structures of O 1s in XPS spectra. See also Figure S4 and Data S3.

(B) The relative abundance of O<sub>NL</sub> to O<sub>L</sub>. See also Figure S4 and Data S3.

(C) The correlation of O<sub>NL</sub> to HO· concentration in the media (n = 3 for HO· concentration). See also Figure S4 and Data S3.

submicron or nanometer particle sizes were mainly embedded in the EPS matrix, suggesting direct contact or a close physical proximity between hyphae and Fe particles. Intriguingly, the fungal hyphae were still intact after 120 h cultivation with hematite. Upon cultivation, fungal biomass increased rapidly over the first 72 h, with or without the presence of hematite (Figure S5), along with the formation of mineral-mycelial aggregates (Figure 5E; Video S1). After 72 h, the fungus produced ~30% more biomass per respired organic carbon in the presence of hematite (Figure S5), suggesting that the presence of hematite provided some benefit to the fungus. To summarize, cryo-SEM imaging, high-resolution 3D volume rendering, and fungal biomass analyses confirmed that the organism was active and capable of the catalytic reactions that we hypothesize confer an advantage to the organism in terms of protection from oxidative stress (Figure 2) and ensuring the acquisition of essential iron (Figure 1).

## DISCUSSION

Maintaining H<sub>2</sub>O<sub>2</sub> concentrations at subtoxic levels is of paramount importance for microbial growth and evolution [2, 17]. We deduce that the formation of FNs during H<sub>2</sub>O<sub>2</sub> production [6, 12] reduces H<sub>2</sub>O<sub>2</sub>-related oxidative stress and hence alleviates potential cytotoxicity [2], allowing for more efficient fungal

growth (Figure S5). Fungi are known to be capable of utilizing hematite as an iron source mainly through exudation (e.g., organic acids or siderophores) [27], extracellular electron transfer [19], or superoxide-mediated Fenton-like reactions [12] and thus may utilize these strategies to help form FNs. Because the fixation, dehydration, and embedding procedure may potentially alter iron distribution in the samples [12, 28], iron localization in the cell as observed by the HAADF-STEM images (white regions in Figures 1G and S2) could be questionable. However, our NanoSIMS data, obtained without any pretreatment of samples, also provided direct evidence demonstrating the presence of intracellular Fe (blue dots in Figure 1F), confirming that iron redistribution may not have been a significant issue in the fixation and dehydration process. The known interactions between fungi and minerals mainly include mineral colonization, effects of metabolite excretion, and cell wall-mineral surface processes [27]; this study has further demonstrated that biogenic ferrihydrite nanoparticles formed through fungal-hematite interactions can act as nanozymes to scavenge hydrogen peroxide for mitigation of potential cytotoxicity. Furthermore, our evidence from various X-ray spectroscopic analyses unequivocally indicated that non-lattice oxygen in the FNs was primarily responsible for the manifested catalytic activity rather than through the conventional mechanisms of iron redox chemistry. Although dissolved

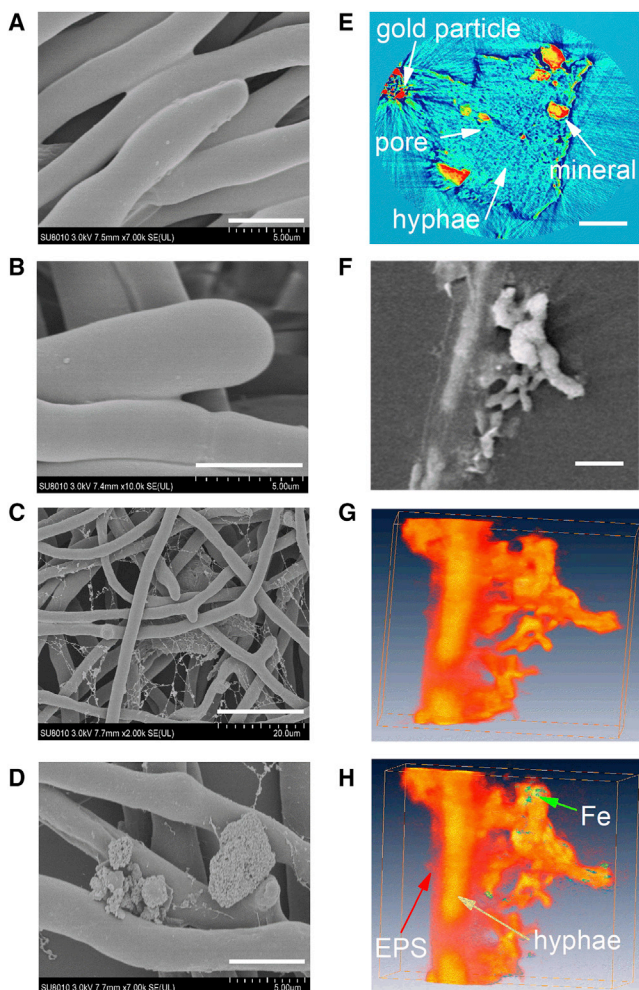


**Figure 5. Morphology of Fungal Hyphae in the Absence or Presence of Iron Nanoparticles**

(A and B) Cryo-SEM images of fungal biomass in the absence of hematite. Scale bar represents 5  $\mu$ m.

(C and D) Cryo-SEM images of fungal biomass in the presence of hematite (120-h cultivation). Scale bars represent 20  $\mu$ m (C) or 5  $\mu$ m (D). See also [Figure S5](#) and [Data S5](#) for changes in fungal biomass.

(E) Synchrotron radiation transmission X-ray microscopy (SR-TXM) image showing the presence of iron minerals, pores, and fungal hyphae in fungal-mineral aggregates (120 h). Scale bar represents 200  $\mu$ m. See also [Video S1](#).

(F) TEM image of fungal-mineral culture samples (120 h). Scale bar represents 5  $\mu$ m.

(G and H) Element-specific 3D volume renderings for the pre-absorption edge of (G) Fe at  $E_1 = 706$  eV and (H) the absorption edge of Fe at  $E_2 = 710$  eV. See also [Videos S2](#) and [S3](#).

Fe has been reported to contribute to the removal of hydrogen peroxide [12, 19], previous observations have also revealed that catalytic reactions on the nanoparticle surfaces were  $\sim$ 50-fold more effective than dissolved Fenton agents [29], which highlights the importance of the electronic structure of surface atoms to the catalytic activities of nanozymes in general.

We further speculate that the utilization of FNs as peroxidase/catalase surrogates may benefit microbial growth (Figure S5) in multiple ways. First, the biogenic formation of nano-ferrihydrate may be energetically more favorable [30]. Protein synthesis in

cells is energy intensive [31], and although not precisely known, some estimated cell costs run at several kJ per g protein synthesized (e.g.,  $\sim$ 5.4 in chickens [32] and  $\sim$ 8.4 in sea urchins [33]). Taking 40 kDa to be an average molecular weight of an enzyme, such energy consumption translates to  $\sim$ 10<sup>5</sup> kJ/mol for peroxidase/catalase synthesis. In comparison, extracellular transformations of minerals may only need to be affected by byproducts of metabolism, such as organic acids, putting little energy burden on normal growth. In our case, the hematite to ferrihydrate transition can take place in water with a theoretical energetic cost of only  $\sim$ 33 kJ/mol [34]. Thus, even with 10% of the efficiency of a natural peroxidase, the FNs can still carry out beneficial catalysis at a fraction of the energy costs required for enzyme synthesis when abundant nanoparticles are produced. Second, because hydroxyl radicals are not only a non-selective strong oxidant but also play a key role in fungal differentiation and pathogen defense mechanisms [6], organisms need to regulate the presence of hydroxyl radicals to maintain an optimal biological concentration while minimizing toxic effects on living cells. The weaker catalytic activity of FNs relative to natural peroxidase [3] and the ensuing moderate production of hydroxyl radicals may aid in this process. Further, the mineral nanoparticles may form physical shields on cell surfaces that would prevent hydroxyl radicals from penetrating [35]. Indeed, both cryo-SEM analyses (Figures 5A–5D) and high-resolution 3D volume renderings (Figures 5G and 5H) showed that the fungal hyphae were intact after cultivation. The results from the growth experiments also indicated that, after 72 h of cultivation, the fungi produced  $\sim$ 30% more biomass per respired organic carbon in the presence of hematite (Figure S5). Third, the formation of hydroxyl radicals (Figure S3) may expedite the breakdown of recalcitrant soil organic matter, such as lignocellulosic residues, to facilitate nutrient acquisition in nutrition-poor environments [19]. Finally, the formation of hydroxyl radicals (Figure S3) during fungus-nanomaterial interactions may play an essential role in alleviating environmental stress by the attenuation of contaminants, e.g., degradation of organic pollutants and transformations of toxic metals [36, 37]. The fungus-nanomaterial interactions reported here resonate with some findings for pioneer plants capable of colonizing metal-rich mine wastes where root-mediated biomineralization controlled zinc bioavailability, and therefore mineral evolution in the rhizosphere, which has implications for phytoremediation techniques [38].

Given the teragram (Tg)-level abundance of mineral nanoparticles in the Earth system [8], it is statistically highly probable for some of them, particularly those of biotic origin, to behave similarly to the FNs as mimetic catalysts. Regardless of the origin of the nanoparticles, over 100 types of natural and engineered nanomaterials have been reported to possess intrinsic enzyme-like catalytic activities [3]. As such, a previously unknown feedback route of microbe-mineral coevolution may have revealed itself in the form of mineral nanozymes that could shed light on long-standing issues, such as the origin and evolution of life by modulating ROS levels. Because more than two-thirds of mineral species in the Earth's surface have biological imprints [39], this current study has emphasized the need for further exploration of microbe-mineral interactions that will improve our understanding of the coevolution of the early geosphere and biosphere.

## STAR★METHODS

Detailed methods are provided in the online version of this paper and include the following:

- **KEY RESOURCES TABLE**
- **RESOURCE AVAILABILITY**
  - Lead Contact
  - Materials Availability
  - Data and Code Availability
- **EXPERIMENTAL MODEL AND SUBJECT DETAILS**
  - Fungal-mineral cultivation
  - Ferrihydrite nanoparticle extraction
- **METHOD DETAILS**
  - Peroxidase-like activity measurement
  - *In situ* detection of O<sub>2</sub><sup>•-</sup>, H<sub>2</sub>O<sub>2</sub> and micro-environmental pH of hyphae
  - Quantification of HO<sup>•</sup> and H<sub>2</sub>O<sub>2</sub> in the medium
  - Correlative SEM and NanoSIMS analyses
  - TEM and cryo-SEM analyses
  - XAS and XPS analyses
  - Three-dimensional volume rendering of the fungal-mineral aggregates
  - Fungal biomass analysis and chemical analysis
- **QUANTIFICATION AND STATISTICAL ANALYSIS**

## SUPPLEMENTAL INFORMATION

Supplemental Information can be found online at <https://doi.org/10.1016/j.cub.2020.05.058>.

## ACKNOWLEDGMENTS

This work was supported by the National Natural Science Foundation of China (grant nos. 41977271, 41830859, 41972041, and 11227902). G.M.G. gratefully acknowledges research support of the Geomicrobiology Group from the Natural Environment Research Council, UK (NE/M010910/1 and NE/M 011275/1). We thank Drs. Xiangzhi Zhang and Lijuan Zhang and Nian Zhang for help and support at beamlines BL08U1-A and BL02B02 at Shanghai Synchrotron Radiation Facility, Wanxia Huang and Qingxi Yuan at 4W1A beamline at Beijing Synchrotron Radiation Facility, and Jian Chen at State Key Laboratory for Mineral Deposits Research, School of Earth Sciences and Engineering, Nanjing University. The authors also thank Owen W. Duckworth for helpful discussions.

## AUTHOR CONTRIBUTIONS

G.-H.Y. and H.H.T. designed the research; G.-H.Y. and Z.-L.C. performed the research; G.-H.Y. and Z.-L.C. analyzed the data; and G.-H.Y., Z.-L.C., A.K., F.-S.S., C.-Q.L., H.H.T., and G.M.G. wrote the paper.

## DECLARATION OF INTERESTS

The authors declare no competing interests.

Received: April 10, 2020

Revised: April 30, 2020

Accepted: May 18, 2020

Published: June 11, 2020

## REFERENCES

1. Gao, L., Zhuang, J., Nie, L., Zhang, J., Zhang, Y., Gu, N., Wang, T., Feng, J., Yang, D., Perrett, S., and Yan, X. (2007). Intrinsic peroxidase-like activity of ferromagnetic nanoparticles. *Nat. Nanotechnol.* 2, 577–583.
2. Chen, Z., Yin, J.-J., Zhou, Y.-T., Zhang, Y., Song, L., Song, M., Hu, S., and Gu, N. (2012). Dual enzyme-like activities of iron oxide nanoparticles and their implication for diminishing cytotoxicity. *ACS Nano* 6, 4001–4012.
3. Wei, H., and Wang, E. (2013). Nanomaterials with enzyme-like characteristics (nanozymes): next-generation artificial enzymes. *Chem. Soc. Rev.* 42, 6060–6093.
4. Michel, F.M., Ehm, L., Antao, S.M., Lee, P.L., Chupas, P.J., Liu, G., Strongin, D.R., Schoonen, M.A.A., Phillips, B.L., and Parise, J.B. (2007). The structure of ferrihydrite, a nanocrystalline material. *Science* 316, 1726–1729.
5. Hochella, M.F., Jr., Lower, S.K., Maurice, P.A., Penn, R.L., Sahai, N., Sparks, D.L., and Twining, B.S. (2008). Nanominerals, mineral nanoparticles, and Earth systems. *Science* 319, 1631–1635.
6. Zhang, J., Miao, Y., Rahimi, M.J., Zhu, H., Steindorff, A., Schiessler, S., Cai, F., Pang, G., Chenthamara, K., Xu, Y., et al. (2019). Guttation capsules containing hydrogen peroxide: an evolutionarily conserved NADPH oxidase gains a role in wars between related fungi. *Environ. Microbiol.* 21, 2644–2658.
7. Cornell, R.M., and Schwertmann, U. (2006). *The Iron Oxides: Structure, Properties, Reactions, Occurrences and Uses*, Second Edition (Wiley), pp. 433–474.
8. Hochella, M.F., Jr., Mogk, D.W., Ranville, J., Allen, I.C., Luther, G.W., Marr, L.C., McGrail, B.P., Murayama, M., Qafoku, N.P., Rosso, K.M., et al. (2019). Natural, incidental, and engineered nanomaterials and their impacts on the Earth system. *Science* 363, eaau8299.
9. Loron, C.C., François, C., Rainbird, R.H., Turner, E.C., Borensztajn, S., and Javaux, E.J. (2019). Early fungi from the Proterozoic era in Arctic Canada. *Nature* 570, 232–235.
10. Heckman, D.S., Geiser, D.M., Eidell, B.R., Stauffer, R.L., Kardos, N.L., and Hedges, S.B. (2001). Molecular evidence for the early colonization of land by fungi and plants. *Science* 293, 1129–1133.
11. Korbekandi, H., Irvani, S., and Abbasi, S. (2009). Production of nanoparticles using organisms. *Crit. Rev. Biotechnol.* 29, 279–306.
12. Yu, G.-H., Chi, Z.-L., Teng, H.H., Dong, H.-L., Kappler, A., Gillings, M.R., Polizzotto, M.L., Liu, C.-Q., and Zhu, Y.-G. (2019). Fungus-initiated catalytic reactions at hyphal-mineral interfaces drive iron redox cycling and biomineralization. *Geochim. Cosmochim. Acta* 260, 192–203.
13. Hansel, C.M., Zeiner, C.A., Santelli, C.M., and Webb, S.M. (2012). Mn(II) oxidation by an ascomycete fungus is linked to superoxide production during asexual reproduction. *Proc. Natl. Acad. Sci. USA* 109, 12621–12625.
14. Aguirre, J., Hansberg, W., and Navarro, R. (2006). Fungal responses to reactive oxygen species. *Med. Mycol.* 44 (Supplement 1), S101–S107.
15. Weber, K.A., Spanbauer, T.L., Wacey, D., Kilburn, M.R., Loope, D.B., and Kettler, R.M. (2012). Biosignatures link microorganisms to iron mineralization in a paleoaquifer. *Geology* 40, 747–750.
16. Baumgartner, J., Morin, G., Menguy, N., Perez Gonzalez, T., Widdrat, M., Cosmidis, J., and Faivre, D. (2013). Magnetotactic bacteria form magnetite from a phosphate-rich ferric hydroxide via nanometric ferric (oxyhydr)oxide intermediates. *Proc. Natl. Acad. Sci. USA* 110, 14883–14888.
17. Winterbourn, C.C. (2008). Reconciling the chemistry and biology of reactive oxygen species. *Nat. Chem. Biol.* 4, 278–286.
18. Melton, E.D., Swanner, E.D., Behrens, S., Schmidt, C., and Kappler, A. (2014). The interplay of microbially mediated and abiotic reactions in the biogeochemical Fe cycle. *Nat. Rev. Microbiol.* 12, 797–808.
19. Jensen, K.A., Jr., Houtman, C.J., Ryan, Z.C., and Hammel, K.E. (2001). Pathways for extracellular Fenton chemistry in the brown rot basidiomycete *Gloeophyllum trabeum*. *Appl. Environ. Microbiol.* 67, 2705–2711.
20. Mueller, D.N., Machala, M.L., Bluhm, H., and Chueh, W.C. (2015). Redox activity of surface oxygen anions in oxygen-deficient perovskite oxides during electrochemical reactions. *Nat. Commun.* 6, 6097.
21. Chen, J.G. (1997). NEXAFS investigations of transition metal oxides, nitrides, carbides, sulfides and other interstitial compounds. *Surf. Sci. Rep.* 30, 1–152.

22. Wang, Z., Mao, X., Chen, P., Xiao, M., Monny, S.A., Wang, S., Konarova, M., Du, A., and Wang, L. (2019). Understanding the roles of oxygen vacancies in hematite-based photoelectrochemical processes. *Angew. Chem. Int. Ed. Engl.* **58**, 1030–1034.
23. Li, Y., Li, Y., Xu, X., Ding, C., Chen, N., Ding, H., and Lu, A. (2019). Structural disorder controlled oxygen vacancy and photocatalytic activity of spinel-type minerals: a case study of ZnFe<sub>2</sub>O<sub>4</sub>. *Chem. Geol.* **504**, 276–287.
24. Strand, J., Kaviani, M., Gao, D., El-Sayed, A.-M., Afanas'ev, V.V., and Shluger, A.L. (2018). Intrinsic charge trapping in amorphous oxide films: status and challenges. *J. Phys. Condens. Matter* **30**, 233001.
25. Jiang, H., Xu, R., Chen, C.-C., Yang, W., Fan, J., Tao, X., Song, C., Kohmura, Y., Xiao, T., Wang, Y., et al. (2013). Three-dimensional coherent x-ray diffraction imaging of molten iron in mantle olivine at nanoscale resolution. *Phys. Rev. Lett.* **110**, 205501.
26. Hunter, R.C., Hitchcock, A.P., Dynes, J.J., Obst, M., and Beveridge, T.J. (2008). Mapping the speciation of iron in *Pseudomonas aeruginosa* biofilms using scanning transmission X-ray microscopy. *Environ. Sci. Technol.* **42**, 8766–8772.
27. Gadd, G.M. (2007). Geomycology: biogeochemical transformations of rocks, minerals, metals and radionuclides by fungi, bioweathering and bioremediation. *Mycol. Res.* **111**, 3–49.
28. Perfumo, A., Elsaesser, A., Littmann, S., Foster, R.A., Kuypers, M.M.M., Cockell, C.S., and Kminek, G. (2014). Epifluorescence, SEM, TEM and nanoSIMS image analysis of the cold phenotype of *Clostridium psychrophilum* at subzero temperatures. *FEMS Microbiol. Ecol.* **90**, 869–882.
29. Voinov, M.A., Sosa Pagán, J.O., Morrison, E., Smirnova, T.I., and Smirnov, A.I. (2011). Surface-mediated production of hydroxyl radicals as a mechanism of iron oxide nanoparticle biotoxicity. *J. Am. Chem. Soc.* **133**, 35–41.
30. Luther, G.W. (2010). The role of one- and two-electron transfer reactions in forming thermodynamically unstable intermediates as barriers in multi-electron redox reactions. *Aquat. Geochem.* **16**, 395–420.
31. Bier, D.M. (1999). The energy costs of protein metabolism: lean and mean on Uncle Sam's team. *The Role of Protein and Amino Acids in Sustaining and Enhancing Performance* (National Academy Press), pp. 109–119.
32. Aoyagi, Y., Tasaki, I., Okumura, J., and Muramatsu, T. (1988). Energy cost of whole-body protein synthesis measured *in vivo* in chicks. *Comp. Biochem. Physiol. A Comp. Physiol.* **91**, 765–768.
33. Pace, D.A., and Manahan, D.T. (2006). Fixed metabolic costs for highly variable rates of protein synthesis in sea urchin embryos and larvae. *J. Exp. Biol.* **209**, 158–170.
34. Navrotsky, A., Mazeina, L., and Majzlan, J. (2008). Size-driven structural and thermodynamic complexity in iron oxides. *Science* **319**, 1635–1638.
35. Sakimoto, K.K., Kornienko, N., Cestellos-Blanco, S., Lim, J., Liu, C., and Yang, P. (2018). Physical biology of the materials–microorganism interface. *J. Am. Chem. Soc.* **140**, 1978–1985.
36. Huang, P.-M., Wang, M.-K., and Chiu, C.-Y. (2005). Soil mineral-organic matter-microbe interactions: impacts on biogeochemical processes and biodiversity in soils. *Pedobiologia (Jena)* **49**, 609–635.
37. Huang, Y., Ren, J., and Qu, X. (2019). Nanozymes: classification, catalytic mechanisms, activity regulation, and applications. *Chem. Rev.* **119**, 4357–4412.
38. Medas, D., De Giudici, G., Casu, M.A., Musu, E., Gianoncelli, A., Iadecola, A., Meneghini, C., Tamburini, E., Sprocati, A.R., Turnau, K., and Lattanzi, P. (2015). Microscopic processes ruling the bioavailability of Zn to roots of *Euphorbia pithyusa* L. pioneer plant. *Environ. Sci. Technol.* **49**, 1400–1408.
39. Hazen, R.M., Papineau, D., Bleeker, W., Downs, R.T., Ferry, J.M., McCoy, T.J., Sverjensky, D.A., and Yang, H. (2008). Mineral evolution. *Am. Mineral.* **93**, 1693–1720.
40. Schwertmann, U., and Cornell, R.M. (2007). *Iron Oxides in the Laboratory: Preparation and Characterization* (Wiley), pp. 121–134.
41. Jiang, B., Duan, D., Gao, L., Zhou, M., Fan, K., Tang, Y., Xi, J., Bi, Y., Tong, Z., Gao, G.F., et al. (2018). Standardized assays for determining the catalytic activity and kinetics of peroxidase-like nanozymes. *Nat. Protoc.* **13**, 1506–1520.
42. Linxiang, L., Abe, Y., Nagasawa, Y., Kudo, R., Usui, N., Imai, K., Mashino, T., Mochizuki, M., and Miyata, N. (2004). An HPLC assay of hydroxyl radicals by the hydroxylation reaction of terephthalic acid. *Biomed. Chromatogr.* **18**, 470–474.
43. Zhou, M., Diwu, Z., Panchuk-Voloshina, N., and Haugland, R.P. (1997). A stable nonfluorescent derivative of resorufin for the fluorometric determination of trace hydrogen peroxide: applications in detecting the activity of phagocyte NADPH oxidase and other oxidases. *Anal. Biochem.* **253**, 162–168.
44. Yu, G., Xiao, J., Hu, S., Polizzotto, M.L., Zhao, F., McGrath, S.P., Li, H., Ran, W., and Shen, Q. (2017). Mineral availability as a key regulator of soil carbon storage. *Environ. Sci. Technol.* **51**, 4960–4969.
45. Xiao, J., He, X., Hao, J., Zhou, Y., Zheng, L., Ran, W., Shen, Q., and Yu, G. (2016). New strategies for submicron characterization the carbon binding of reactive minerals in long-term contrasting fertilized soils: Implications for soil carbon storage. *Biogeosciences* **13**, 3607–3618.
46. Newsome, L., Lopez Adams, R., Downie, H.F., Moore, K.L., and Lloyd, J.R. (2018). NanoSIMS imaging of extracellular electron transport processes during microbial iron(III) reduction. *FEMS Microbiol. Ecol.* **94**, 5033680.
47. Mergelov, N., Mueller, C.W., Prater, I., Shorkunov, I., Dolgikh, A., Zazovskaya, E., Shishkov, V., Krupskaya, V., Abrosimov, K., Cherkinsky, A., and Goryachkin, S. (2018). Alteration of rocks by endolithic organisms is one of the pathways for the beginning of soils on Earth. *Sci. Rep.* **8**, 3367.
48. Li, H., Hu, S., Polizzotto, M.L., Chang, X., Shen, Q., Ran, W., and Yu, G. (2016). Fungal biomineralization of montmorillonite and goethite to short-range-ordered minerals. *Geochim. Cosmochim. Acta* **191**, 17–31.
49. Fdez-Gubieda, M.L., Muela, A., Alonso, J., García-Prieto, A., Olivi, L., Fernández-Pacheco, R., and Barandiarán, J.M. (2013). Magnetite biomineralization in *Magnetospirillum gryphiswaldense*: time-resolved magnetic and structural studies. *ACS Nano* **7**, 3297–3305.
50. Suntivich, J., Hong, W.T., Lee, Y.-L., Rondinelli, J.M., Yang, W., Goodenough, J.B., Dabrowski, B., Freeland, J.W., and Shao-Horn, Y. (2014). Estimating hybridization of transition metal and oxygen states in perovskites from O K-edge X-ray absorption spectroscopy. *J. Phys. Chem. C* **118**, 1856–1863.
51. Ren, G., Zhang, N., Feng, X., Zhang, H., Yu, P., Zheng, S., Zhou, D., Tian, Z., and Liu, X. (2020). Photon-in/photon-out endstation for studies of energy materials at beamline 02B02 of Shanghai Synchrotron Radiation Facility. *Chin. Phys. B* **29**, 016101.
52. Ravel, B., and Newville, M. (2005). ATHENA, ARTEMIS, HEPHAESTUS: data analysis for X-ray absorption spectroscopy using IFEFFIT. *J. Synchrotron Radiat.* **12**, 537–541.
53. Risch, M., Stoerzinger, K.A., Han, B., Regier, T.Z., Peak, D., Sayed, S.Y., Wei, C., Xu, Z., and Shao-Horn, Y. (2017). Redox processes of manganese oxide in catalyzing oxygen evolution and reduction: an *in situ* soft X-ray absorption spectroscopy study. *J. Phys. Chem. C* **121**, 17682–17692.
54. Yuan, Q., Zhang, K., Hong, Y., Huang, W., Gao, K., Wang, Z., Zhu, P., Gelb, J., Tkachuk, A., Hornberger, B., et al. (2012). A 30 nm-resolution hard X-ray microscope with X-ray fluorescence mapping capability at BSRF. *J. Synchrotron Radiat.* **19**, 1021–1028.
55. Tian, D., Jiang, Z., Jiang, L., Su, M., Feng, Z., Zhang, L., Wang, S., Li, Z., and Hu, S. (2019). A new insight into lead (II) tolerance of environmental fungi based on a study of *Aspergillus niger* and *Penicillium oxalicum*. *Environ. Microbiol.* **21**, 471–479.
56. Amstaeetter, K., Borch, T., and Kappler, A. (2012). Influence of humic acid imposed changes of ferrihydrite aggregation on microbial Fe(III) reduction. *Geochim. Cosmochim. Acta* **85**, 326–341.

STAR★METHODS

KEY RESOURCES TABLE

REAGENT or RESOURCE	SOURCE	IDENTIFIER
Chemicals, Peptides, and Recombinant Proteins		
TPA	Toyko	Cat#100-21-0
hTPA	Toyko	Cat#636-94-2
Amplex red	Invitrogen	Cat#119171-73-2
HRP	Sigma	Cat#CH0203
Ferrozine	Sigma	Cat#69898-45-9
NBT	Sigma	Cat#298-83-9
DAB	Sigma	Cat#91-95-2
Deposited Data		
Raw and analyzed datasets, Data S1–S6	This study	<a href="https://doi.org/10.17632/wtck8dgdgm.2">https://doi.org/10.17632/wtck8dgdgm.2</a>
Experimental Models: Organisms/Strains		
<i>Trichoderma guizhouense</i> NJAU 4742	Natural isolate from a cucumber root in a cropping system, Nanjing, Jiangsu, China	N/A
Software and Algorithms		
ImageJ	NIH	<a href="https://imagej.nih.gov/ij/">https://imagej.nih.gov/ij/</a>
OpenMIMS	OpenMIMS ImageJ plugin	<a href="http://www.nrims.hms.harvard.edu/NRIMS_ImageJ.php">http://www.nrims.hms.harvard.edu/NRIMS_ImageJ.php</a>
Excel	Microsoft	<a href="https://products.office.com/en-gb/excel">https://products.office.com/en-gb/excel</a>
Origin9.1	OriginLab	<a href="https://www.originlab.com/">https://www.originlab.com/</a>
SPSS16	IBM	<a href="https://www.ibm.com/products/spss-statistics">https://www.ibm.com/products/spss-statistics</a>
CasaXPS software (version 2.3)	Casa Software Ltd	<a href="https://www.casaxps.com/berlin">https://www.casaxps.com/berlin</a>
TXM Reconstructor	Xradia TXM Reconstructor software (v. 8.1.7546)	N/A
ATHENA software	IFEFFIT 1.2.11	<a href="http://cars9.uchicago.edu/ifeffit/Downloads">http://cars9.uchicago.edu/ifeffit/Downloads</a>

RESOURCE AVAILABILITY

Lead Contact

Further information and requests for resources should be directed to and will be fulfilled by the Lead Contact, Guang-Hui Yu ([yuguanghui@tju.edu.cn](mailto:yuguanghui@tju.edu.cn)).

Materials Availability

This study did not generate new unique reagents.

Data and Code Availability

The raw datasets generated or analyzed during this study, referred to as Data S1–S6 in the figure legends, are available at Mendeley Data (<https://doi.org/10.17632/wtck8dgdgm.2>).

## EXPERIMENTAL MODEL AND SUBJECT DETAILS

### Fungal-mineral cultivation

The experimental fungus *Trichoderma guizhouense* NJAU 4742 was originally provided by Dr. Jian Zhang (Nanjing Agricultural University) [6]. All experiments were performed in triplicate at 28°C in the dark using potato dextrose agar (PDA) medium [6] with the addition of hematite to the desired final concentrations. Hematite was synthesized by mixing 2L of 0.002 M HNO<sub>3</sub> (98°C) with 16.16 g Fe(NO<sub>3</sub>)<sub>3</sub>·9H<sub>2</sub>O (0.02 M Fe) followed by 7 days of aging at 98°C [40]. At the conclusion of the synthesis procedure [40], the suspension was dialyzed with deionized water for 3 days to remove impurities and the collected precipitates were vacuum freeze-dried. The fungal-mineral cultivation experiments were initiated when the liquid medium containing 0.1% (w/v) hematite was inoculated with *T. guizhouense* conidia (10<sup>4</sup> cells mL<sup>-1</sup>) and incubated in a shaking incubator (170 rpm) at 28°C.

### Ferrihydrite nanoparticle extraction

Mineral-mycelium aggregate samples, taken at different incubation times (i.e., 0, 24, 48, 72, 96 and 120-h), were first centrifuged at 8000 × g RCF for 5 min to produce mineral pellets that were subsequently washed with Milli-Q water three times, re-suspended to the original volumes using ultrasound at 40 kHz and 400 W for 20 min, and centrifuged again at 10000 × g RCF for 30 min. The supernatant and the mineral pellets produced after the second centrifugation were vacuum freeze-dried to collect FNs in EPS and the reacted parental hematite, respectively.

## METHOD DETAILS

### Peroxidase-like activity measurement

The peroxidase-like activity assays were carried out in 2-mL tubes using 10 μL of 5 mg mL<sup>-1</sup> TMB solution in DMSO as the substrate. Each tube contained one mL of test solution containing either 50 ng horseradish peroxidase (HRP) or 1 mg mineral phase in 0.2 M NaAc-HAc buffer (pH 3.6). The mineral phases were synthetic ferrihydrite, synthetic hematite, FNs and reacted hematite fractions, un-fractionated samples (i.e., reacted hematite + FNs), and abiotic control (i.e., the hematite being exposed to a pH 3.6). Synthetic ferrihydrite was prepared by dissolving 40 g Fe(NO<sub>3</sub>)<sub>3</sub>·9H<sub>2</sub>O in 500 mL deionized water, followed by the addition of 330 mL 1 M KOH [40]. To test the effect of pH variations on the catalytic activity of hematite, an abiotic control experiment was conducted by adding 0.2 M NaAc-HAc buffer, that is a value similar to the pH environments of the FNs in the cultivation experiments (Figure S3). A blue color was observed after input of H<sub>2</sub>O<sub>2</sub> (to a final concentration of 50 mM) at 28°C. The solution mixtures were used for absorbance measurements at 652 nm every 15 s up to 20 min. A sample without addition of H<sub>2</sub>O<sub>2</sub> or the TMB solution was used as the control.

Nanozyme activity (units) were calculated as follows [41]:

$$b_{\text{nanozyme}} = V / (\epsilon \times l) \times (\Delta A / \Delta t) \quad (\text{Equation 1})$$

where  $b_{\text{nanozyme}}$  is the activity of the nanozyme expressed in catalytic units that are defined as the amount of nanozyme that catalytically produces 1 μmol of product per min at 28°C;  $V$  is the total volume of reaction solution (μL);  $\epsilon$  is the molar absorption coefficient of the colorimetric substrate (typically maximized at 39000 M<sup>-1</sup> cm<sup>-1</sup> at 652 nm for TMB);  $l$  is the path length of light in the cuvette (cm). The quantity  $\Delta A / \Delta t$  is the initial rate of change in absorbance at 652 nm min<sup>-1</sup>.

### In situ detection of O<sub>2</sub><sup>•-</sup>, H<sub>2</sub>O<sub>2</sub> and micro-environmental pH of hyphae

Extracellular ROS and its spatial distribution were detected using stains that precipitate on reaction with ROS [13]. *T. guizhouense*, grown on PDA plates with an initial pH of 5.6, was flooded with the desired stains, NBT chloride for O<sub>2</sub><sup>•-</sup> and DAB for H<sub>2</sub>O<sub>2</sub>, respectively. The NBT assay (a mixture of 2.5 mM NBT chloride (Sigma, St Louis, MO, USA) and 5 mM 3-(N-morpholino) propanesulfonate-NaOH at pH 7.6) reacts with O<sub>2</sub><sup>•-</sup> to form a blue precipitate, whereas the DAB assay (2.5 mM DAB and 5 μM purpurogallin unit/mL of horseradish peroxidase (type VI, Sigma) in potassium phosphate buffer at pH 6.9) forms a brown precipitate on reaction with H<sub>2</sub>O<sub>2</sub>. For both assays, the plates were first incubated with the stains for ~30 min in the dark, decanted to remove excess reagents, further incubated for an additional 4 h, and finally imaged using a stereomicroscope (Leica DM 5000B). The molecular probe SNARF4F (Invitrogen, Paisley, UK) was used at a 5 μM concentration to determine the pH of hypha using confocal laser scanning microscopy (CLSM) [12].

### Quantification of HO<sup>•</sup> and H<sub>2</sub>O<sub>2</sub> in the medium

Terephthalic acid (TPA, non-fluorescent) stock solution (Tokyo, Japan) was added to samples to a final concentration of 2.5 mM. The fluorescent product that traps HO<sup>•</sup>, 2-hydroxyl TPA (HTPA), was quantified using an Agilent 1260 Infinity high-performance liquid chromatography (HPLC) system (Agilent Technologies, Germany) equipped with a Fluorescence Detector (G1321B) and a reverse-phase C18 column (Develosil ODS-UG5, 4.6 mm × 250 mm, Nomura Chemical, Japan). The concentration of HTPA was used to estimate the cumulative HO<sup>•</sup> concentration [42].

A microtiter plate assay with a detection limit of 5 p mol using 2 μM amplex red (AR) and 1 kU L<sup>-1</sup> HRP as the fluorescence reagent was employed to quantify the H<sub>2</sub>O<sub>2</sub> content [43]. In the presence of HRP, H<sub>2</sub>O<sub>2</sub> reacts with AR with a 1:1 stoichiometry to produce

fluorescent resorufin which has absorption and fluorescence emission maxima at 563 and 587 nm, respectively. Since this method is only effective at circumneutral pH (~7.5–8.5) [43], we mixed 1 mL of sample with 10 mM phosphate buffer to adjust the pH to ~8 prior to measurements.

### Correlative SEM and NanoSIMS analyses

Fungal-mineral aggregates were dispersed in ethanol and dropped onto a silicon wafer. Then, the silicon wafer (with samples on it) was air-dried and gold-coated prior to analysis. SEM (Zeiss EVO18) observation was performed with a 20-kV accelerating potential. For NanoSIMS (Cameca 50L) analyses, the gold coating layer (~10 nm) and possible contamination of the sample surface were first pre-sputtered using a high primary beam current [44, 45]. Secondary ions  $^{12}\text{C}^{14}\text{N}^-$ ,  $^{16}\text{O}^-$  and  $^{56}\text{Fe}^{16}\text{O}^-$  were simultaneously collected by electron multipliers with an electronic dead time of 44 ns. The presence of the  $^{12}\text{C}^{14}\text{N}^-$  ion was interpreted as representing organic matter, while that of  $^{16}\text{O}^-$  and  $^{56}\text{Fe}^{16}\text{O}^-$  were interpreted as minerals and Fe, respectively [44, 46, 47]. The charging effect resulting from nonconductive mineral particles was compensated through use of an electron flood gun. Composite multi-element images were constructed from NanoSIMS images using ImageJ (version 1.45) with the OpenMIMS ([http://www.nrims.hms.harvard.edu/NRIMS\\_ImageJ.php](http://www.nrims.hms.harvard.edu/NRIMS_ImageJ.php)) plugin.

### TEM and cryo-SEM analyses

Fungal-mineral aggregates were dispersed in water, dropped onto carbon-coated copper grids, and air-dried. TEM images were recorded using a JEM-1400 PLUS microscope at an accelerating voltage of 120 keV. The mean particle size ( $\langle D \rangle$ ) and the number (N) of nanoparticles were obtained from TEM imaging and particle-size distribution analysis using ImageJ (NIH) [48, 49].

To locate the nanoparticles in samples, fungal-mineral aggregates after 120-h cultivation were fixed in 2% glutaraldehyde in 0.1 M cacodylate buffer (CB) at pH 7.4 and room temperature for 1 h, washed three times in CB, and post-fixed in 1% osmium tetroxide in CB for 1 h at room temperature. The product material was then embedded in 2.5% (w/v) agarose and dehydrated in a graded ethanol series (30%, 50%, 70%, 90%, and 100%) for 30 min at each step before embedding in Epon resin by standard procedure [28]. Ultrathin sections (70 nm- and 30 nm- for electron microscopy) were cut on a Leica ultramicrotome using a diamond knife (Diatome), transferred onto carbon-coated films on copper grids, and stained for 10 min using 1% uranyl acetate in water. HRTEM images, HAADF-STEM, EDS, and SAED were collected using a FEI Tecnai F20 microscope.

Samples were prepared in a liquid nitrogen cooled-cryo preparation system (PP3010) that allows operation at temperatures down to  $-190^\circ\text{C}$ . The preparation chamber was maintained at high vacuum and fitted with a cold stage on which the sample rested during manipulation (such as cold fracturing, sublimation, and carbon coating). Once prepared, the sample was transferred to the cold stage in the SEM (Hitachi SU8010) through a chamber port for further analysis under cryogenic conditions.

### XAS and XPS analyses

XAS measurements were performed using beamline BL02B02 of the SiP·ME<sup>2</sup> platform at the Shanghai Synchrotron Radiation Facility (SSRF) in the surface sensitive TEY mode. This mode corresponds to a probe depth of approximately 10 nm [50]. The bending magnet beamline provided photons with energy range from 50 to 2000 eV. The photon flux was about  $10^{11}$  photons  $\text{s}^{-1}$  and the energy resolving power was up to 13000. The beam size at sample was set to  $150\ \mu\text{m} \times 50\ \mu\text{m}$  [51]. Samples (FNs, and hematite before and after reaction) were ground into fine powders and mounted on indium foil. A gold-coated screen was used to measure the incident beam intensity ( $I_0$ ). XAS spectra were collected by measuring the sample current and normalizing to  $I_0$ . The spectral energy was varied from 700 to 730 eV in 0.1 eV steps (dwell time 1 s) for the Fe L edge, and 520 to 560 eV in 0.2 eV steps (dwell time 2 s) for the O K-edge. Experiments were carried out at room temperature in an ultrahigh vacuum chamber with a base pressure better than  $1 \times 10^{-9}$  Torr. All XAS spectra normalization was carried out using ATHENA software [52]. The background was removed from the spectra by fitting a line to the pre-edge range between 520 and 524 eV for oxygen and between 703 and 706 eV for iron. The peaks were fitted by Gaussian curves using the “multiple peak fit” tool in Origin 9.1 [53].

XPS data were recorded using a PHI5000 Versa Probe (ULVAC-PHI) equipped with an Al K $\alpha$  source (1486.6 eV). The C 1s signal centered at 284.8 eV was used as an internal reference for the absolute binding energy. Data processing and peaks fitting were carried out using CasaXPS (version 2.3) software.

### Three-dimensional volume rendering of the fungal-mineral aggregates

The fungal-mineral aggregates obtained after 66 h cultivation were analyzed using synchrotron radiation X-ray Nano-CT at beamline 4W1A of the Beijing Synchrotron Radiation Facility (BSRF). Small gold particle fiducial markers were placed on top of the sample to correct sample drift during the 3D reconstruction. The micro-CT ( $\mu$ -CT) experiments were performed using a hard X-ray transmission X-ray microscope (TXM). The imaging process of TXM was as follows: an elliptically shaped capillary condenser was used to focus the incident X-rays onto the sample, and a zone-plate objective was used to magnify the sample images which were finally recorded by a  $1024 \times 1024$  CCD camera. The actual pixel size on the projected images was 64 nm after  $45 \times$  magnification of X-rays by the zone-plate and  $20 \times$  magnification of visible light by the camera lens. Additionally, a phase ring was placed on the back focal plane of the zone-plate to provide Zernike phase contrast [54]. The sample on a pin was placed in a holder in the vacuum chamber and rotated from  $-90^\circ$  to  $90^\circ$  with rotational steps of  $0.5^\circ$  and an exposure time of 15 s at a photon energy of 8 keV. A total of 361 raw images were

acquired, amounting to about 2 h for one sample. Results were obtained after additional steps of data processing included background deduction, alignment, and computed tomography reconstruction using the software packages TXM Controller and TXM Reconstructor.

To obtain high-resolution 3D structural information of hyphae and iron minerals, fungal-mineral aggregates after cultivation for 66 h were dispersed in water and then divided into two portions. The dispersed hyphae were dropped on a copper grid and air-dried. Then, the air-dried sample was placed in a vacuum chamber and analyzed by elemental specific X-ray Nano-CT at the BL08U1-A beamline of SSRF in Shanghai, China. X-rays were focused by an elliptical capillary condenser. Coupled with a micro-zone plate, the whole system can perform absorption imaging with X-ray energies: the pre-absorption edge of iron at  $E_1 = 706$  eV and the absorption edge of iron at  $E_2 = 710$  eV, to scan the sample from  $-69^\circ$  to  $69^\circ$  with a spatial resolution of 30 nm and exposure time of 2 ms [25]. In total, a tilt series of 27 images were collected. Each individual X-ray image in the tilt series was phased to obtain a high resolution 2D image. The series of the 2D images was aligned to the tilt axis with the center of mass technique, and was then reconstructed to obtain a 3D image by the equally sloped tomography method [25].

### Fungal biomass analysis and chemical analysis

Mycelia were dispersed by ultrasound, washed with Milli-Q water, and collected by filtration through a  $0.45\ \mu\text{m}$  polytetrafluoroethylene (PTFE) filter, followed by oven drying ( $65^\circ\text{C}$ ) before being ground into powder. The organic carbon and nitrogen content of the powdered biomass was analyzed using a vario MACRO cube elemental analyzer (Elementar) and calibrated using a sulfanilamide standard (Elemental Microanalysis, Germany) with 41.81 wt.% carbon [55].

Medium samples were centrifuged at  $10000 \times g$  RCF for 5 min, filtered through a  $0.45\ \mu\text{m}$  pore size PTFE filter, and analyzed by inductively coupled plasma-atomic emission spectroscopy (Agilent 710/715 ICP-AES) for dissolved Fe. The concentration of  $\text{Fe}^{2+}$  was then measured by the ferrozine assay [56]. Briefly, one mL of the samples was added to 1 mL of 0.1 M HCl and extracted for 15 min. The mixture was centrifuged and the supernatants were collected for determination of total  $\text{Fe}^{2+}$ . For the analysis of the dissolved  $\text{Fe}^{2+}$ , one mL of the samples was taken and centrifuged to obtain the supernatants. Structural  $\text{Fe}^{2+}$  included both sorbed  $\text{Fe}^{2+}$  and particulate  $\text{Fe}^{2+}$ , and its concentration was obtained by subtracting dissolved  $\text{Fe}^{2+}$  from total  $\text{Fe}^{2+}$ . For FTIR analysis, samples were prepared as a mixture of 1 mg freeze-dried ferrihydrite nanoparticles and 100 mg potassium bromide (KBr, IR grade), and this mixture was then ground and homogenized to obtain FTIR spectra using a Nicolet 370 FTIR spectrometer. Zeta potential, a measure of the surface charge of ferrihydrite nanoparticles, was quantified by a Malvern Zetasizer (Nano Z, Malvern, UK).

### QUANTIFICATION AND STATISTICAL ANALYSIS

Statistical differences between data were assessed using one-way analysis of variance (ANOVA) and windows-based SPSS software (version 16.0) (SPSS). Significance was determined using one-way ANOVA followed by Tukey's HSD post hoc tests, where conditions of normality and homogeneity of variance were met. Means  $\pm$  SD ( $n = 3$ ) in Figures and Tables indicate significant differences between treatments at  $p < 0.05$ .